JVST A
Journal of Vacuum Science & Technology A

Target ion and neutral spread in high power impulse magnetron sputtering

Cite as: J. Vac. Sci. Technol. A **41**, 013002 (2023); https://doi.org/10.1116/6.0002292
Submitted: 15 October 2022 • Accepted: 17 November 2022 • Published Online: 16 December 2022

H. Hajihoseini, N. Brenning, M. Rudolph, et al.

ARTICLES YOU MAY BE INTERESTED IN

Investigation of the magnetron balancing effect on the ionized flux fraction and deposition rate of sputtered titanium species for the high-power impulse magnetron sputtering pulses of different lengths
Journal of Vacuum Science & Technology A **41**, 013003 (2023); https://doi.org/10.1116/6.0002309

Operating modes and target erosion in high power impulse magnetron sputtering
Journal of Vacuum Science & Technology A **40**, 043005 (2022); https://doi.org/10.1116/6.0001919

On the population density of the argon excited levels in a high power impulse magnetron sputtering discharge
Physics of Plasmas **29**, 023506 (2022); https://doi.org/10.1063/5.0071887

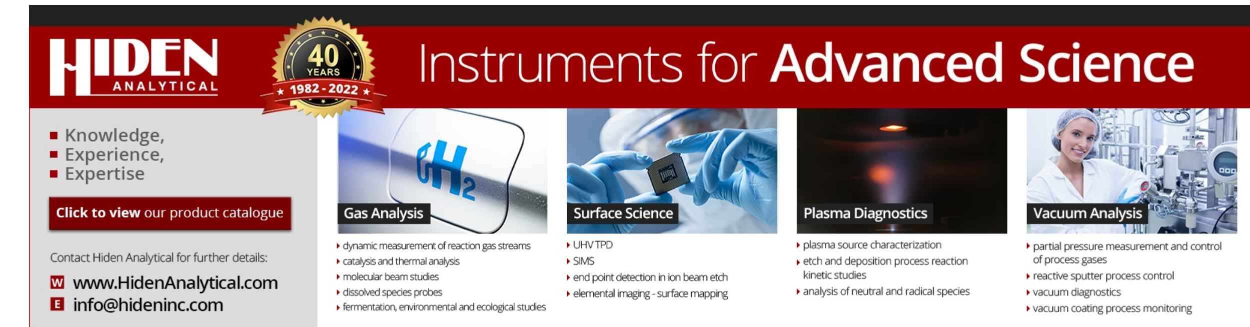

© 2022 Author(s).

Target ion and neutral spread in high power impulse magnetron sputtering

Cite as: J. Vac. Sci. Technol. A **41**, 013002 (2023); doi: 10.1116/6.0002292
Submitted: 15 October 2022 · Accepted: 17 November 2022 ·
Published Online: 16 December 2022

View Online

Export Citation

CrossMark

H. Hajihoseini,[1] N. Brenning,[2,3] M. Rudolph,[4] M. A. Raadu,[2] D. Lundin,[3] J. Fischer,[3] T. M. Minea,[5] and J. T. Gudmundsson[2,6]

AFFILIATIONS

[1]Industrial Focus Group XUV Optics, MESA+ Institute for Nanotechnology, University of Twente, Drienerlolaan 5, 7522 NB Enschede, The Netherlands
[2]Space and Plasma Physics, School of Electrical Engineering and Computer Science, KTH Royal Institute of Technology, SE-100 44 Stockholm, Sweden
[3]Plasma and Coatings Physics Division, IFM-Materials Physics, Linköping University, SE-581 83 Linköping, Sweden
[4]Leibniz Institute of Surface Engineering (IOM), Permoserstraße 15, 04318 Leipzig, Germany
[5]Laboratoire de Physique des Gaz et Plasmas—LPGP, UMR 8578 CNRS, Université Paris–Sud, Université Paris–Saclay, 91405 Orsay Cedex, France
[6]Science Institute, University of Iceland, Dunhaga 3, IS-107 Reykjavik, Iceland

ABSTRACT

In magnetron sputtering, only a fraction of the sputtered target material leaving the ionization region is directed toward the substrate. This fraction may be different for ions and neutrals of the target material as the neutrals and ions can exhibit a different spread as they travel from the target surface toward the substrate. This difference can be significant in high power impulse magnetron sputtering (HiPIMS) where a substantial fraction of the sputtered material is known to be ionized. Geometrical factors or transport parameters that account for the loss of produced film-forming species to the chamber walls are needed for experimental characterization and modeling of the magnetron sputtering discharge. Here, we experimentally determine transport parameters for ions and neutral atoms in a HiPIMS discharge with a titanium target for various magnet configurations. Transport parameters are determined to a typical substrate, with the same diameter (100 mm) as the cathode target, and located at a distance 70 mm from the target surface. As the magnet configuration and/or the discharge current are changed, the transport parameter for neutral atoms ξ_{tn} remains roughly the same, while transport parameters for ions ξ_{ti} vary greatly. Furthermore, the relative ion-to-neutral transport factors, ξ_{ti}/ξ_{tn}, that describe the relative deposited fractions of target material ions and neutrals onto the substrate, are determined to be in the range from 0.4 to 1.1.

© 2022 Author(s). All article content, except where otherwise noted, is licensed under a Creative Commons Attribution (CC BY) license (http://creativecommons.org/licenses/by/4.0/). https://doi.org/10.1116/6.0002292

I. INTRODUCTION

The magnetron sputtering discharge[1] is a widely used plasma discharge-driven physical vapor deposition technique,[2] where the film-forming species are released from a solid target, the discharge cathode, by an ion-driven sputter process. Magnetron sputter deposition is a highly successful deposition technique that is utilized in a range of industries. Magnetron sputtering is based on maintaining a static magnetic field, which effectively increases the residence time of electrons in the vicinity of the cathode target surface.[1,3] In the planar magnetron sputter configuration, the confining magnetic field is provided by concentrically placing a central magnet and an outer edge magnet, with antiparallel magnetization, behind the cathode target. The electron confinement results in a dense plasma that provides ions to the sputter process. This is apparent in the discharge operation, since, in the presence of such a confining magnetic field, the discharge voltage and the working gas pressure are lower, making the discharge more energy-efficient and the deposition rate substantially higher, compared to the nonmagnetized dc diode sputtering process.[1,4] The magnetron sputtering discharge exists in a number of configurations, and various waveforms are applied to drive the discharges in order to be suitable for a range of diverse applications.[1,5,6]

When the magnetron sputtering discharge is driven by high power unipolar pulses of low repetition frequency and low duty cycle, it is referred to as a high power impulse magnetron sputtering (HiPIMS) discharge.[1,7,8] HiPIMS delivers high degree of ionization of the sputtered material to the deposition process[9–11] while being compatible with existing magnetron sputtering deposition systems. As a consequence, in HiPIMS deposition, the flux of sputtered species, i.e., the film-forming material, is composed of both ion and neutral species. In an HiPIMS discharge with a titanium target, the ionized density fraction of the sputtered material has been shown to be higher than 90%.[12] The increased ionization of the sputtered species translates into a higher ionized flux fraction.[10] The higher ionized flux fraction leads to superior properties of the deposited films,[13] which are realized, in particular, due to improved crystallinity and enhanced film mass density.[14] Additionally, the increased ionization of the sputtered species can improve coating uniformity when depositing on complex surfaces and the uniformity of the coating is often of utmost importance. As an example, it has been demonstrated that titanium films deposited by HiPIMS on the inner (concave) and outer (convex) surfaces of a bowl-shaped workpiece exhibited better uniformity in terms of crystal texture, microhardness, and microstructure than that of dc magnetron sputtering (dcMS) deposited films.[15] Also, it has previously been shown that nickel films deposited obliquely by HiPIMS deposition exhibit up to 40% better thickness uniformity than dc magnetron sputter deposited films under the same tilt angle.[16]

In general, the spatiotemporal density distribution of neutrals and ions of the sputtered species are not the same, as has indeed been observed experimentally in a number of studies.[17–21] In particular, the ions and neutrals of the sputtered species exhibit a different spread as they travel from the target surface toward the substrate. In this context, the term spread refers to the cone of neutrals and ions as they leave the ionization region (IR). The spread of ions is expected to be larger compared to that of neutrals, as they have typically larger scattering cross sections and are influenced by electric fields and instabilities[22] as well as electric fields from ionization waves, also known as spokes.[23,24] The spokes are known to become more pronounced for stronger magnetic fields and higher peak discharge currents.[25] Under these conditions, ions could be subjected to a stronger lateral deflection away from their initial axial direction that they obtain as neutrals when being sputtered from the target, which has indeed been demonstrated by Panjan *et al.*[26]

In the original description of the target material pathways model of the high power impulse magnetron sputter process, Christie[27] introduced geometrical factors, termed transport parameters ξ_{tn} and ξ_{ti} for the target material neutrals and ions, respectively, to underline the fact that only a fraction of the sputtered target material leaving the ionization region is directed toward the substrate in magnetron sputter deposition. The spread of the neutrals and ions can be different and, therefore, this fraction is different for neutrals and ions of the sputtered species. Transport parameters are defined such that $0 \leq \xi_{tn} \leq 1$ and $0 \leq \xi_{ti} \leq 1$, for neutrals and ions, respectively, where 1 means that all species are directed toward the substrate. Consequently, the relative ion-to-neutral transport factor, ξ_{ti}/ξ_{tn}, describes the relative deposited fractions of target material ions and neutrals onto the substrate. Note that this ratio is termed f_{Ω}^{-1} in some previous works (see, e.g., Refs. 28 and 29).

In a recent study, we measured the sideways (lateral, i.e., parallel to the target surface) deposition rate and ionized flux fraction in a HiPIMS discharge and compared to a dcMS discharge with a titanium target, while the magnetic field strength $|\mathbf{B}|$ and the degree of magnetic balancing were varied.[30] This study was performed using a planar circular magnetron assembly. We found, for both dcMS and HiPIMS operation, that a significant flux of the film-forming material is directed perpendicular to the target surface and that the sideways deposition rate decreases with increasing axial distance from the target surface. However, it was observed that the sideways deposition rate is always high in dcMS operation and always found to be lower for HiPIMS operation. Furthermore, it was found that there are significantly more ions traveling laterally in the HiPIMS discharge. A comparison of the total lateral as well as axial fluxes across the entire investigated plasma volume between the target and the substrate position allows us to revise the estimates of lateral over axial flux fractions for different magnet configurations and discharge currents. The measurements, therefore, allow us to determine transport parameters ξ_{tn} and ξ_{ti} and the relative ion-to-neutral transport factor, ξ_{ti}/ξ_{tn}, and to explore how the determined parameters vary with magnet configuration and discharge current.

Here, we determine transport parameters ξ_{ti} and ξ_{tn} at the substrate position for the titanium neutrals and titanium ions, respectively, in a HiPIMS discharge for various magnet configurations. In Sec. II, we discuss the concept of transport parameters, how they are defined, and discuss a few examples and values used in past modeling work and experimental analysis. The experimental apparatus and method are discussed in Sec. III. In Sec. IV, we discuss the results of the findings and some implications. The findings are summarized in Sec. V.

II. TRANSPORT PARAMETERS

Transport parameters depend on the geometry of the sputter system, the magnetic field configuration, the discharge current, and the size of the areas where the flux parameters, the deposition rate, and the ionized flux fraction, are determined. For the concept of transport parameters, the area for both the deposition and loss of film-forming species has to be defined. Transport parameters are the probability that a certain species leaving the ionization region deposits onto the substrate. For HiPIMS operation, this ratio needs to be determined for both ions and neutral species.

To better understand the concept of transport parameters, let us look at a few examples. For a half-sphere substrate that covers the whole diffusion region, we have $\xi_{tn} = \xi_{ti} = 1$, and, therefore, the ratio is $\xi_{ti}/\xi_{tn} = 1$. Similarly, if the ions exhibit the same spread as the neutral atoms, then the ratio $\xi_{ti}/\xi_{tn} = 1$ at all locations within the diffusion region. However, if the ions are generally deflected more sideways (away from the central axis) than the sputtered neutral flux, then the ratio ξ_{ti}/ξ_{tn} depends on the position: close to the central axis $\xi_{ti}/\xi_{tn} < 1$, and at positions sufficiently far away from the axis, $\xi_{ti}/\xi_{tn} > 1$. On the contrary, if the ions are deflected toward the axis these two inequalities become reversed. As a consequence of these examples, we should not expect the same ratios ξ_{ti}/ξ_{tn} at two different locations: above the center of

© Author(s) 2022

the target or above racetrack. Please note that transport parameters ξ_{ti} and ξ_{tn} are not global parameters, such as the internal discharge parameters ionization probability α_t and back-attraction probability β_t,[24] but depend on both the substrate size and orientation as follows.

Here, we define transport parameters to an imagined or virtual substrate, circular with the same diameter as the target, and placed facing the target, parallel to the target surface, located at some distance from the target surface. We regard this as a "typical substrate" and use the notations ξ_{ti}^{sub} for transport parameters for ions of the target material, and ξ_{tn}^{sub} for transport parameters for neutrals of the target material. For large substrates, such as this "typical substrate," transport parameters are averages over the substrate area. The volume of interest between the target surface and the imagined substrate is a cylinder. In this case, the area of the sidewall of a cylinder is denoted $A_{sidewall}$ and the area of the end of the cylinder (i.e., of the substrate) is denoted A_{sub}. A transport parameter for neutral titanium atoms ξ_{tn} is then defined as

$$\xi_{tn}^{sub} = \frac{\text{neutral flux onto } A_{sub}}{\text{neutral flux onto } A_{sub} + \text{neutral flux onto } A_{sidewall}}$$

and a transport parameter for titanium ions ξ_{ti} is defined by

$$\xi_{ti}^{sub} = \frac{\text{ion flux onto } A_{sub}}{\text{ion flux onto } A_{sub} + \text{ion flux onto } A_{sidewall}}.$$

Note that for a cylinder $A_{sidewall}/A_{sub} = 2(Z/R)$, where Z is the length and R is the radius of the cylinder.

In their extension of the target material pathway model, Vlček and Burcalová[31] used two different values for the relative ion-to-neutral transport factor $\xi_{ti}/\xi_{tn} = 0.5$ and 1.0. In an earlier study, we related the measured quantities, the deposition rate, and ionized flux fraction, to the ionization probability α_t and the back-attraction probability of the sputtered species β_t,[11] where the ratio ξ_{ti}/ξ_{tn} was assumed to be one. Later, we revised the original analytical model[11] by including the ratio of transport parameters for ions and neutrals, which we assumed to have a value of $\xi_{ti}/\xi_{tn} = 0.5$.[24] In the ionization region model (IRM), we have also assumed a value of $\xi_{ti}/\xi_{tn} = 0.5$.[24,28] This value was estimated based on measurements by Britun *et al.*[18] and this assumption was grounded on assuming different scatter cones for neutrals and ions in the discharge.[24,28] Note that the ion-to-neutral transport parameter ratio used in the IRM is not necessarily the same as for a typical substrate. The IRM code calculates the fluxes in and out of the IR in the target vicinity and the length of the cylinder is typically 2–4 cm and does generally not include the substrate region located in the diffusion region. Furthermore, in the IRM, the deposition on the end plate is assumed to be uniform and often the flux parameters are determined by a quartz crystal microbalance (QCM) in one particular location.

III. EXPERIMENTAL APPARATUS AND METHOD

The experiments were performed in a custom-built cylindrical vacuum chamber (height 50 cm and diameter 45 cm) made of stainless steel. A base pressure of 4×10^{-6} Pa was achieved using a turbomolecular pump backed by a roughing pump. The working gas pressure was maintained at 1 Pa by injecting 50 sccm argon into the chamber and adjusting a butterfly valve located between the chamber and the turbomolecular pump. The deposition system was equipped with a circular 4 in. diameter VTec magnetron assembly (Gencoa, Liverpool, UK) with titanium target, which along with a probe holder was mounted on movable bellows. Therefore, it was possible to perform lateral as well as axial scans with high precision. A schematic of the magnetron sputtering system, including the magnetron assembly and a probe holder, is shown in Fig. 1. A detailed description of the experimental setup is given elsewhere.[11,30]

The absolute magnetic field strength $|\mathbf{B}|$ and the degree of magnetic balancing in the vicinity of the cathode target were varied by independently displacing the center magnet (C) and the outer ring magnet at the target edge (E) using two micrometer screws located on the outer side of the magnetron assembly. The various configurations are referred to by using the displacement (in millimeters) of each magnet from the back of the target. Therefore, the notation C0E0 refers to a magnet configuration where the center and outer magnets touch the backing plate (zero displacement, i.e., the strongest magnetic field above the target).

The axial and the sideways deposition rate and ionized flux fraction were determined for seven different magnet arrangements or magnet configurations.[11,30] Table I shows the magnet configurations and related HiPIMS discharge parameters that were determined experimentally. The pulse length was 100 μs, and the average power was maintained at 300 W for all the magnet

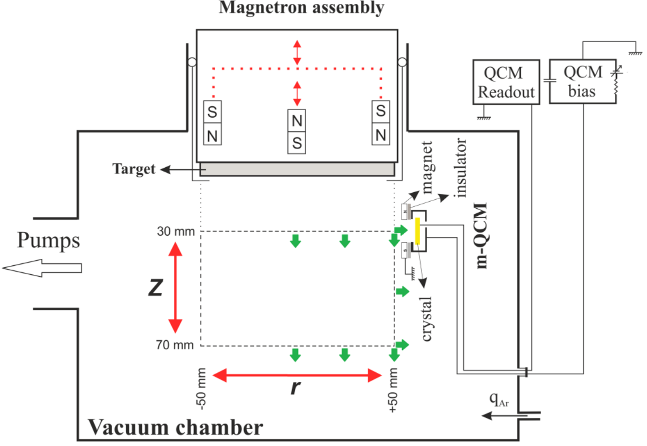

FIG. 1. Schematic of the magnetron sputtering system. The magnetron assembly and the probe holder with the m-QCM (ion meter) are mounted on movable bellows that can be controlled with millimeter precision. The red arrows indicate linear motion, and the dashed rectangle displays the limits of the investigated (cylindrical) volume. The green arrows show the position and direction of measurements using the ion meter. The absolute magnetic field strength $|\mathbf{B}|$ as well as the geometry of the magnetic field (degree of balancing) above the magnetron target can be varied by displacing the center magnet (C) and the outer ring magnet at the target edge (E) using two micrometer screws located on the outer side of the magnetron assembly.

© Author(s) 2022

TABLE I. Operating parameters for running HiPIMS discharges in fixed voltage mode with 4 in. diameter titanium target. The average discharge power was always kept at 300 W by varying the pulse frequency, the pulse length was kept at 100 μs. The magnetic field strength B_{rt} was measured 11 mm above the racetrack, and z_{null} is the location of the magnetic null point.

	Magnet		HiPIMS fixed voltage		
Notation	$B_{r,rt}$ (Gauss)	z_{null} (mm)	V_D (V)	$I_{D,peak}$ (A)	f_{pulse} (Hz)
C0E0	238	66	625	80	54
C5E5	161	59	625	40	97
C10E10	111	52	625	12	450
C5E0	181	53	625	53	80
C10E0	137	43	625	31	134
C0E5	217	70	625	54	76
C0E10	213	74	625	35	115

configurations studied, by varying the repetition frequency, while the discharge voltage was maintained at 625 V. We term this approach, to maintain constant average power while the magnet configuration is varied, fixed voltage mode. When varying the magnet configuration while maintaining fixed discharge voltage the discharge current varies greatly. The choice of operating mode and its influence on the flux parameters have been explored in a recent study.[32] Please note that Table I shows variations in three parameters, $B_{r,rt}$, z_{null}, and $I_{D,peak}$. This limits our possibilities to pinpoint the physical reason for observed variations in transport parameters. For a practical example, Table I shows that the C0E0 configuration has both the strongest magnetic field and the highest discharge current. We will see below that the ion transport parameter for this configuration is among the lowest—but we cannot from the data available disentangle whether the basic physical reason is the strong magnetic field or the high discharge current.

An ion meter (or gridless quartz crystal-microbalance (QCM)/m-QCM) was used to determine the flux parameters. The gridless ion meter consists of magnetic shielding, a grounded casing, and a QCM sensor, which can be biased to achieve charge selectivity. The device is described in detail by Kubart et al.[9] The ion meter gives either the deposition rate from ions and neutrals or from neutrals only by varying a voltage applied to the biased top QCM electrode, allowing for fast (roughly 1 min) determination of the ionized fraction of the material flux to the sensor head. The magnetron assembly and the probe holder, with the m-QCM attached, were mounted on movable bellows controlled with millimeter precision, as shown in Fig. 1. It was possible to perform the measurement at various locations within the discharge chamber, both with the m-QCM (ion meter) facing the target surface and placing it perpendicular to the target surface.

For this current analysis, the lateral flux, parallel to the target surface, was recorded at three locations $(r, z) = (50, 30)$ mm, $(r, z) = (50, 50)$ mm, and $(r, z) = (50, 70)$ mm. The axial flux was recorded 70 mm from the target surface over the center $((r, z) = (0, 70))$, racetrack $((r, z) = (25, 70))$, and the edge of the target $((r, z) = (50, 70))$ as well as 30 mm from the target surface over the center $((r, z) = (0, 30))$, racetrack $((r, z) = (25, 30))$, and the edge of the target $((r, z) = (50, 30))$.

The deposition rates due to neutrals and ions of the sputtered species were determined at the three locations on the end surface and the sidewall of the cylinder. These flux rates were determined for both titanium atoms and titanium ions. In the first step, the local measurements were linearly fitted and integrated over the whole region of interest. The axial deposition rate due to neutrals (onto a virtual substrate) was calculated by

$$R_{tn}^{sub} = 2\pi \int_0^R r\mathcal{R}_{tn}^{sub}(r)\,dr, \tag{1}$$

where R is the radius of the virtual substrate and $\mathcal{R}_{tn}^{sub}(r)$ is a linear fit through the lateral variation of the local deposition rates of neutrals onto the virtual surface A_{sub}. Similarly, the deposition rate due to ions is

$$R_{ti}^{sub} = 2\pi \int_0^R r\mathcal{R}_{ti}^{sub}(r)\,dr, \tag{2}$$

where $\mathcal{R}_{ti}^{sub}(r)$ is a linear fit through the local deposition rates due to ions onto the virtual surface A_{sub}.

The deposition rate on the lateral walls due to neutrals was calculated using

$$R_{tn}^{wall} = 2\pi R \int_0^Z \mathcal{R}_{tn}^{wall}(z)\,dz, \tag{3}$$

where $\mathcal{R}_{tn}^{wall}(z)$ is the linear fit to the local deposition rates due to neutrals on the cylindrical sidewalls and Z is the location of the end surface, and similarly the deposition rate due to ions on the sidewalls is

$$R_{ti}^{wall} = 2\pi R \int_0^Z \mathcal{R}_{ti}^{wall}(z)\,dz, \tag{4}$$

where $\mathcal{R}_{ti}^{wall}(z)$ is the linear fit to the local deposition rates due to ions on the cylindrical sidewalls. Note that to determine the linear fits for $\mathcal{R}_{ti}^{wall}(z)$ and $\mathcal{R}_{tn}^{wall}(z)$, we have linearly extrapolated the lateral deposition rates down to the cathode target surface. With decreasing distance to the cathode target surface, the deposition rate is assumed to increase, and, therefore, the contribution to the lateral deposition rates onto a virtual wall increases strongly close to the cathode surface. This extrapolation down to the target surface creates the biggest uncertainty in determining the transport parameters.

Transport parameters for neutrals are then calculated as

$$\xi_{tn}^{sub} = \frac{R_{tn}^{sub}}{R_{tn}^{sub} + R_{tn}^{wall}} \tag{5}$$

© Author(s) 2022

and for ions, the transport parameter is calculated as

$$\xi_{\rm ti}^{\rm sub} = \frac{R_{\rm ti}^{\rm sub}}{R_{\rm ti}^{\rm sub} + R_{\rm ti}^{\rm wall}}. \quad (6)$$

IV. RESULTS AND DISCUSSION

Figure 2 shows the measured local deposition rates for neutrals and ions, both axially and laterally, for all the magnet configurations explored. The axial deposition rates due to neutrals at $z = 70$ mm generally increase as one moves from the center of the virtual substrate and towards the edge [Fig. 2(a)], while the axial ion deposition rates peak over the racetrack [Fig. 2(b)]. The axial deposition rates for neutrals depend very much on the magnet configuration and are higher when the magnets are further away from the back of the cathode target (weaker magnetic field), while the deposition rates for ions show a somewhat different dependence on magnet configuration. The dependence of the axial deposition rate on the magnet configuration and the magnetic field strength has been the subject of earlier studies.[11,32] The increased deposition rate with lower magnetic field strength is well documented and has been known from the early days of the development of the HiPIMS technique.[33,34] The lateral deposition rate decreases as one moves away from the target surface location axially—this is true for both neutrals [Fig. 2(c)] and ions [Fig. 2(d)]. The lateral deposition rates due to neutrals is highest when the magnets are closest to the back of the cathode target, while the deposition rates for ions are the lowest in this case. The data shown in Fig. 2 are used to calculate the transport parameters for both ions and neutrals following the procedure described in Sec. III. In Fig. 2, the linear fits to the measured data are also shown.

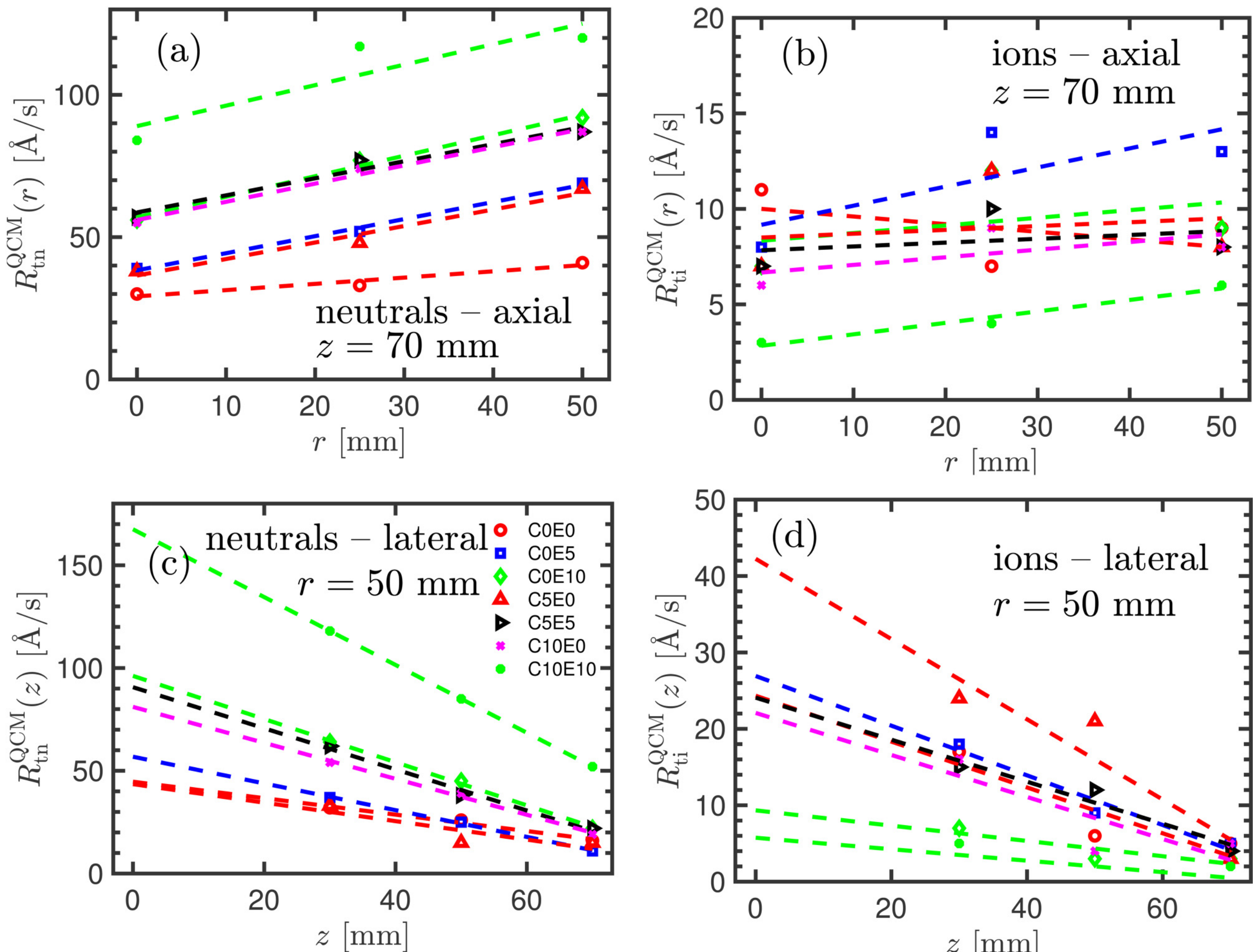

FIG. 2. Measured deposition rate for (a) neutrals axially at $z = 70$ mm, (b) ions axially at $z = 70$ mm, (c) neutrals laterally at $r = 50$ mm, and (d) ions laterally at $r = 50$ mm.

© Author(s) 2022

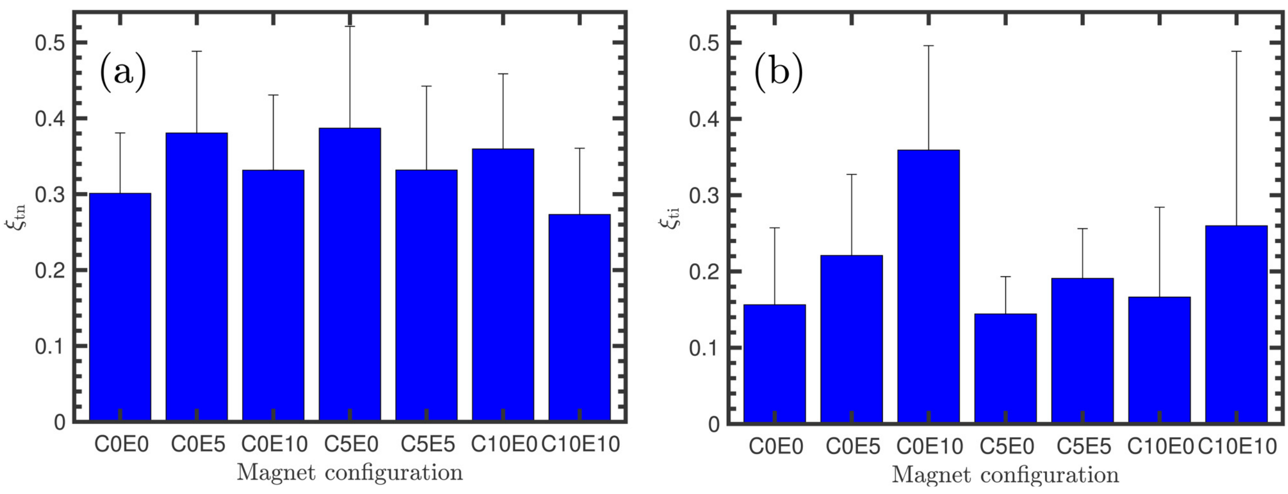

FIG. 3. Transport parameters for (a) neutral titanium atoms ξ_{tn}, and for (b) titanium ions ξ_{ti}, for the various magnet configurations, determined assuming a 70 mm long cylinder. Note that the magnetic field strength decreases from left to right.

Transport parameters are determined by calculating the ratio of the deposition rate onto a virtual area of the size of the target located 70 and 30 mm from the target surface to the deposition rate onto the sides of a cylinder that is 70 and 30 mm long, respectively. 70 mm is the typical substrate distance in this system and 30 mm is the edge of the IR (see the discussion of transport parameters in the IRM at the end of Sec. II). The measured transport parameters for neutral titanium ξ_{tn} determined using Eq. (5) for the various magnet configurations for a 70 mm long cylinder are shown in Fig. 3(a). Transport parameters for neutral titanium atoms ξ_{tn} do not vary much with the magnet configuration and are in the range from 0.27 to 0.38 and have an average value of 0.34 with a standard deviation of 0.04.

Transport parameters for ions ξ_{ti} calculated using Eq. (6) for a 70 mm long cylinder are shown in Fig. 3(b). It is apparent that transport parameters for titanium ions ξ_{ti} vary significantly with the magnet configuration and/or discharge current. For most of the magnet configurations, ion transport parameters are smaller than for the neutrals. Transport parameters for neutral titanium atoms ξ_{tn} for the various magnet configurations and 30 mm long cylinder are shown in Fig. 4(a) and transport parameters for titanium ions

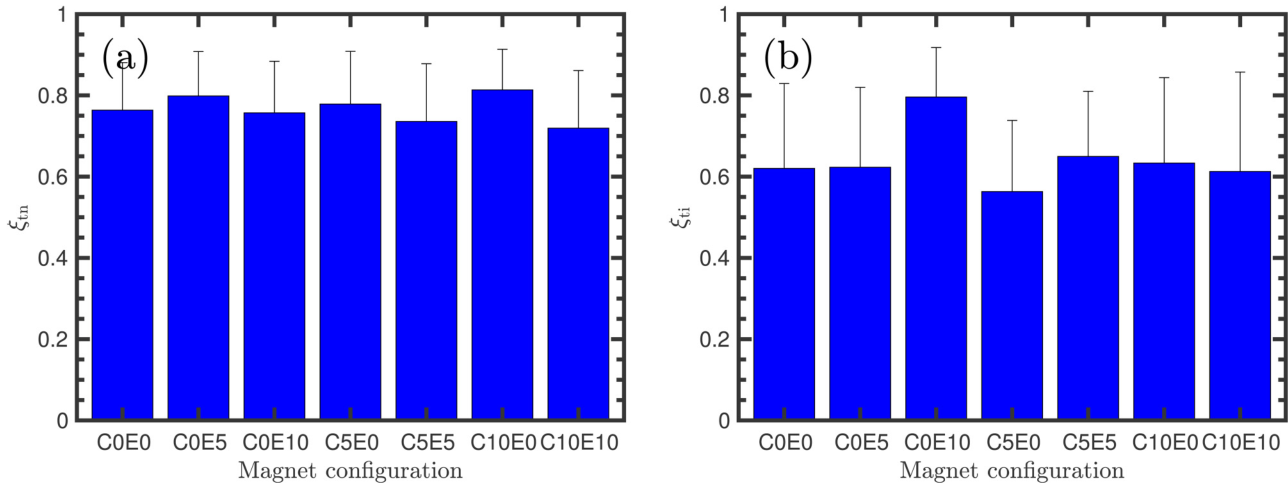

FIG. 4. Transport parameters for (a) neutral titanium atoms ξ_{tn}, and for (b) titanium ions ξ_{ti}, for the various magnet configurations, determined assuming a 30 mm long cylinder. Note that the magnetic field strength decreases from left to right.

© Author(s) 2022

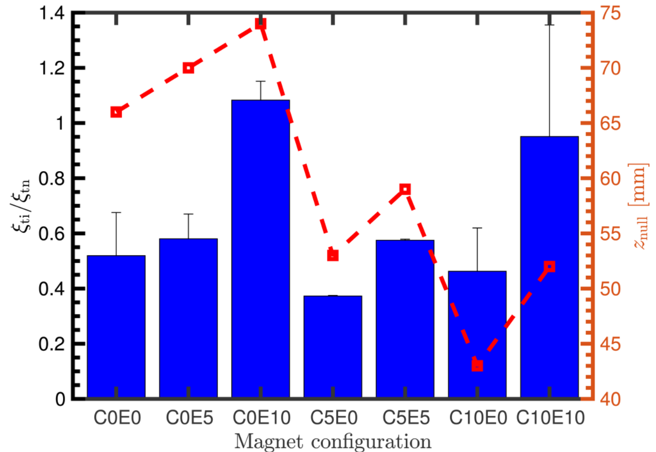

FIG. 5. Ratio of the transport parameter for titanium ions and the transport parameter for neutral titanium atoms ξ_{ti}/ξ_{tn} for the various magnet configurations, determined assuming a 70 mm long cylinder. The location of the magnetic null z_{null} is also shown. Note that the magnetic field strength decreases from left to right.

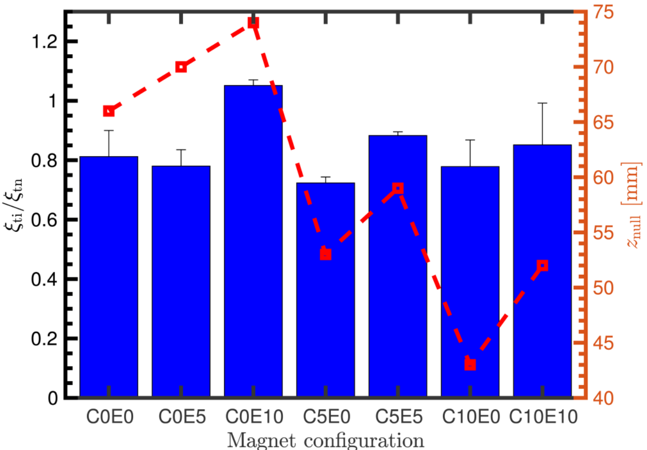

FIG. 6. Ratio of the transport parameter for titanium ions and the transport parameter for neutral titanium atoms ξ_{ti}/ξ_{tn} for the various magnet configurations, determined assuming a 30 mm long cylinder. The location of the magnetic null z_{null} is also shown. Note that the magnetic field strength decreases from left to right.

ξ_{ti} are shown in Fig. 4(b). Transport parameters for both neutral titanium atoms and titanium ions for a 30 mm long cylinder are larger than for a 70 mm cylinder. This is because more neutrals and ions reach the virtual end surface if the cylinder is shorter. Transport parameters are also calculated using a linear fit to the measured data in the range 30–70 mm and then assuming that the lateral transport decreases linearly from the value at 30 mm to zero at the target surface. We assume that this approach gives the upper limit on the calculated transport parameters for both neutrals and ions. This value is indicated by the error bars in Figs. 3(a) and 3(b) and Figs. 4(a) and 4(b). Our reported value are calculated assuming a linear fit and extrapolation with increasing lateral flux closer to the target is the lower limit. We see that the choice of fitting and extrapolation does, for most of the cases, not have a significant influence on the overall results.

Due to the large variation in the transport parameters for ions seen in Fig. 3(b), the relative ion-to-neutral transport factor ξ_{ti}/ξ_{tn} varies greatly depending on the magnet configuration and discharge current, as seen in Fig. 5 for a 70 mm long cylinder. In Fig. 5, the location of the magnetic null z_{null} is added onto the graph. We see that the variation in z_{null} follows the variation in the relative ion-to-neutral transport factor ξ_{ti}/ξ_{tn}, and essentially ξ_{ti}, as the magnetic configuration and the discharge current are varied. Thus, it is clear that the degree of magnetic unbalance has an influence on the transport parameter for ions and, therefore, the relative ion-to-neutral transport factor ξ_{ti}/ξ_{tn}. The average value $\langle\xi_{ti}/\xi_{tn}\rangle$ is 0.64 with a standard deviation of 0.25. The ratio of the transport parameter for titanium ions and neutral titanium atoms ξ_{ti}/ξ_{tn} for the various magnet configurations, determined assuming a 30 mm long cylinder is shown in Fig. 6. The average value is 0.84 with a standard deviation of 0.11. The ratios of the transport parameters at 30 mm have somewhat higher values than at 70 mm.

Figure 7 shows transport parameters for titanium ions ξ_{ti} for a 70 mm long cylinder, versus the location of the magnetic null point z_{null}. The transport parameter for titanium ions is grouped by constant $z_{gap} = z_C + z_E$ the sum of the two distances of the central and

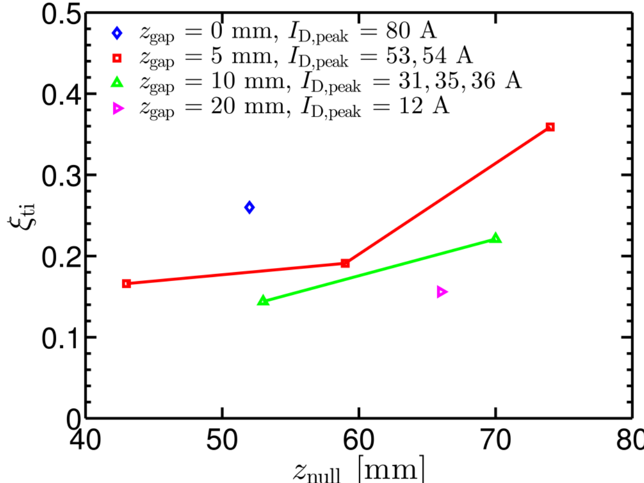

FIG. 7. Transport parameters for titanium ions ξ_{ti}, for a 70 mm long cylinder, vs the location of the magnetic null point z_{null}. The transport parameter for titanium ions is grouped by constant $z_{gap} = z_C + z_E$, which is the sum of the two distances of the central and the edge magnet from the rear of the target, z_C and z_E, respectively.

© Author(s) 2022

the edge magnet from the rear of the target, z_C and z_E, respectively. This parameter has been found to be a similarity parameter, meaning that discharges having equal z_{gap} have similar discharge properties.[35] Here, discharges with equal z_{gap} have approximately the same peak discharge current.

Despite the limited data set, we see some indication that ξ_{ti} increases with increasing z_{null} for a constant value of z_{gap} and/or $I_{D,peak}$. This would mean that a more balanced magnetron assembly delivers more ions onto the substrate rather than expelling them sideways. We also see from Fig. 7 that for a constant z_{null}, ξ_{ti} increases for decreasing values of z_{gap} and/or increasing values for $I_{D,peak}$.

A. Implication of the ξ_{ti}/ξ_{tn} on the estimates of the internal discharge parameters

Earlier, we derived equations for the sputter-rate-normalized deposition rate F_{sput} and the ionized flux fraction $F_{ti,flux}$ as functions of the internal discharge parameters ionization probability α_t and back-attraction probability β_t.[24] The normalized deposition rate and the ionized flux fraction are typically determined using an ion meter that is placed in one particular location. The sputter-rate-normalized deposition rate is

$$F_{sput} = (1-\alpha_t) + \left(\frac{\xi_{ti}}{\xi_{tn}}\right)\alpha_t(1-\beta_t) \tag{7}$$

and for the special case when $\xi_{ti} = \xi_{tn}$, this expression reduces to a reduction in the deposition rate by a factor $(1-\alpha_t\beta_t)$, in agreement with Bradley *et al.*,[36] which we used in our earlier work.[11] The ionized flux fraction at the substrate becomes

$$F_{ti,flux} = \left(1 + \frac{\xi_{tn}}{\xi_{ti}}\frac{1-\alpha_t}{\alpha_t(1-\beta_t)}\right)^{-1} \tag{8}$$

when no additional ionization of the sputtered species occurs in the diffusion region. A more general equation for the ionized flux fraction for the sputtered species was derived by Vlček and Burcalová.[31] For the case when $\xi_{ti} = \xi_{tn}$, Eq. (8) reduces to

$$F_{ti,flux} = \frac{\alpha_t(1-\beta_t)}{1-\alpha_t\beta_t}, \tag{9}$$

which was used in our earlier work to analyze an experimental discharge.[11]

Reformulating Eqs. (7) and (8) yields equations for the ionization probability of the sputtered species[24]

$$\alpha_t = 1 - F_{sput}(1 - F_{ti,flux}) \tag{10}$$

and the ion back-attraction probability of the sputtered species

$$\beta_t = \frac{F_{sput}F_{ti,flux}\left(1-\frac{\xi_{tn}}{\xi_{ti}}\right) - F_{sput} + 1}{1 - F_{sput}(1-F_{ti,flux})}. \tag{11}$$

Equation (11) can be rearranged to be written in terms of the ion escape probability

$$\frac{\xi_{ti}}{\xi_{tn}}(1-\beta_t) = \frac{F_{sput}F_{ti,flux}}{1-F_{sput}(1-F_{ti,flux})}, \tag{12}$$

where the measured flux parameters are placed on the right hand side, and the left hand side is the multiplication of the ion escape probability and the ion-to-neutral transport parameter ratio. Equations (10) and (11) present a more general form of the equations for the internal discharge parameters α_t and β_t than those in our previous work,[11] where we assumed $\xi_{ti} = \xi_{tn}$.

We see that the ionization probability given by Eq. (10) does not depend on the transport parameters. This leaves the back-attraction probability β_t as the parameter of interest and to be explored further. Recall that the high back-attraction probability is the main reason for the low deposition rate in HiPIMS operation.[27] In our earlier work, when analyzing the experimental discharge, we determined the ionization probability and the back-attraction probability assuming $\xi_{ti} = \xi_{tn}$.[11] As we now have determined ξ_{ti}/ξ_{tn} for various magnet configurations, we can reanalyze the data. A parameter of very practical importance, which we focus on here, is the ion escape probability $(1-\beta_t)$,[37,38] given by Eq. (12). In Fig. 8, we compare the ion escape probability $(1-\beta_t)$, calculated using the measured ξ_{ti}/ξ_{tn} determined for the 70 mm case, and shown in Fig. 5, to the ion escape probability determined assuming $\xi_{ti}/\xi_{tn} = 0.5$ and $\xi_{ti}/\xi_{tn} = 1.0$ onto an ion meter. We note that assuming $\xi_{ti}/\xi_{tn} = 1.0$, which is what we assumed in our earlier study,[11] gives the lowest, and rather constant, ion escape probability, while using the measured (as well as assuming $\xi_{ti}/\xi_{tn} = 0.5$) gives higher ion escape probability for most cases. However, there

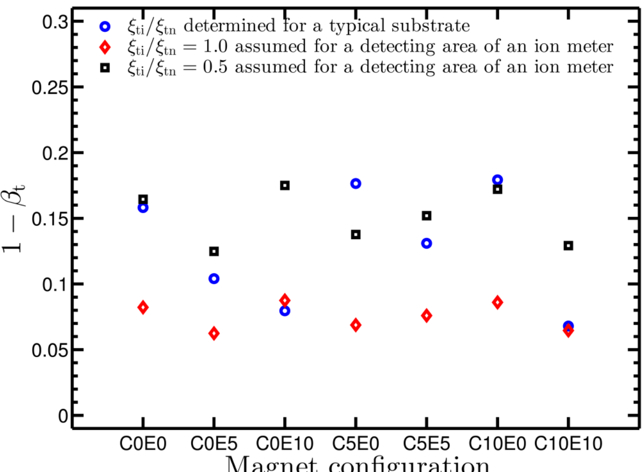

FIG. 8. Ion escape probability for the various magnet configurations comparing the measured ratio of the transport parameter for titanium ions and the transport parameter for neutral titanium atoms for a typical surface 70 mm away from the target ξ_{ti}/ξ_{tn}, to assuming $\xi_{ti}/\xi_{tn} = 0.5$ and $\xi_{ti}/\xi_{tn} = 1.0$ to the detecting area of an ion meter.

© Author(s) 2022

is also more variation in the ion escape probability with the magnet configuration when the measured value is used. Indeed, we note that the back-attraction probability β_t and the location of the magnetic null z_{null} follow a similar pattern.

In earlier studies, we have modeled the discharges studied here using the Ionization Region Model (IRM).[24,29,35] Based on experimental observations by Britun *et al.*[17,18], we have assumed a value of $\xi_{ti}/\xi_{tn} = 0.5$ independent of the magnetic field topology, which should be compared to the 30 mm case as the ionization region is typically assumed to extend 2–4 cm from the target surface. The results shown in Fig. 6 indicate that this was a fair estimate on average. However, there are noticeable deviations.

V. CONCLUSIONS

We have determined transport parameters onto a typical substrate for titanium ions and neutrals in an a HiPIMS discharge. Transport parameters for the neutrals depend only weakly on the magnetic field configuration, while transport parameters for the ions depend more strongly on the magnet configuration and discharge current. Consequently, the ratio of the transport parameter for titanium ions and the transport parameter for neutral titanium atoms ξ_{ti}/ξ_{tn} varies greatly and appears to be in the range 0.4–1.1. The lower values of ξ_{ti}/ξ_{tn} are correlated with a lower back-attraction probability (or higher ion escape probability) and the scatter in the values with varying magnet configuration leads to increased variation in the ion escape probability. We find that the ratio of the transport parameters ξ_{ti}/ξ_{tn} and the back-attraction probability for ions of the sputtered species β_t exhibits a similar pattern as the location of the magnetic null. A larger sideways spread, away from a normal target position, can preliminarily be correlated to the magnetic field strength, the degree of magnetic unbalance, and the discharge current. However, in the present data set, these three parameters are correlated in such a way that it is not possible to disentangle these trends; this will be the subject of future experimental investigations.

ACKNOWLEDGMENTS

This work was partially supported by the Icelandic Research Fund (Grant No. 196141), the Free State of Saxony and the European Regional Development Fund (Grant No. 100336119), and the Swedish Government Strategic Research Area in Materials Science on Functional Materials at Linköping University (Faculty Grant SFO-Mat-LiU No. 2009-00971).

AUTHOR DECLARATIONS

Conflict of Interest

The authors have no conflicts to disclose.

Author Contributions

H. Hajihoseini: Conceptualization (lead); Data curation (lead); Formal analysis (equal); Investigation (equal); Methodology (equal); Writing – original draft (equal); Writing – review & editing (equal). **N. Brenning:** Investigation (equal); Validation (equal); Writing – original draft (equal); Writing – review & editing (equal). **M. Rudolph:** Data curation (equal); Formal analysis (equal); Writing – original draft (equal); Writing – review & editing (equal). **M. A. Raadu:** Formal analysis (equal); Writing – review & editing (equal). **D. Lundin:** Data curation (lead); Funding acquisition (equal); Supervision (equal); Validation (equal); Writing – review & editing (equal). **J. Fischer:** Validation (equal); Writing – review & editing (equal). **T. M. Minea:** Validation (equal); Writing – review & editing (equal). **J. T. Gudmundsson:** Data curation (equal); Formal analysis (equal); Project administration (equal); Supervision (equal); Validation (equal); Writing – original draft (lead); Writing – review & editing (lead).

DATA AVAILABILITY

The data that support the findings of this study are available from the corresponding author upon reasonable request.

REFERENCES

[1] J. T. Gudmundsson, Plasma Sources Sci. Technol. **29**, 113001 (2020).
[2] J. T. Gudmundsson, A. Anders, and A. von Keudell, Plasma Sources Sci. Technol. **31**, 083001 (2022).
[3] D. Krüger, K. Köhn, S. Gallian, and R. P. Brinkmann, Phys. Plasmas **25**, 061207 (2018).
[4] R. K. Waits, J. Vac. Sci. Technol. **15**, 179 (1978).
[5] P. J. Kelly and R. D. Arnell, Vacuum **56**, 159 (2000).
[6] U. Helmersson, M. Lattemann, J. Bohlmark, A. P. Ehiasarian, and J. T. Gudmundsson, Thin Solid Films **513**, 1 (2006).
[7] J. T. Gudmundsson, N. Brenning, D. Lundin, and U. Helmersson, J. Vac. Sci. Technol. A **30**, 030801 (2012).
[8] *High Power Impulse Magnetron Sputtering: Fundamentals, Technologies, Challenges and Applications*, edited by D. Lundin, T. Minea, and J. T. Gudmundsson (Elsevier, Amsterdam, 2020).
[9] T. Kubart, M. Čada, D. Lundin, and Z. Hubička, Surf. Coat. Technol. **238**, 152 (2014).
[10] D. Lundin, M. Čada, and Z. Hubička, Plasma Sources Sci. Technol. **24**, 035018 (2015).
[11] H. Hajihoseini, M. Čada, Z. Hubička, S. Ünaldi, M. A. Raadu, N. Brenning, J. T. Gudmundsson, and D. Lundin, Plasma **2**, 201 (2019).
[12] J. Bohlmark, J. Alami, C. Christou, A. P. Ehiasarian, and U. Helmersson, J. Vac. Sci. Technol. A **23**, 18 (2005).
[13] K. Sarakinos and L. Martinu, in *High Power Impulse Mangetron Sputtering: Fundamentals, Technologies, Challenges and Applications*, edited by D. Lundin, T. Minea, and J. T. Gudmundsson (Elsevier, Amsterdam, 2020), pp. 333–374.
[14] M. Samuelsson, D. Lundin, J. Jensen, M. A. Raadu, J. T. Gudmundsson, and U. Helmersson, Surf. Coat. Technol. **202**, 591 (2010).
[15] D. Xie, L. J. Wei, H. Y. Liu, K. Zhang, Y. X. Leng, D. T. A. Matthews, and R. Ganesan, Surf. Coat. Technol. **442**, 128192 (2022).
[16] H. Hajihoseini, M. Kateb, S. Ingvarsson, and J. T. Gudmundsson, Beilstein J. Nanotechnol. **10**, 1914 (2019).
[17] N. Britun, M. Palmucci, S. Konstantinidis, and R. Snyders, J. Appl. Phys. **117**, 163302 (2015).
[18] N. Britun, M. Palmucci, S. Konstantinidis, and R. Snyders, J. Appl. Phys. **117**, 163303 (2015).
[19] J. Hnilica, P. Klein, P. Vašina, R. Snyders, and N. Britun, J. Appl. Phys. **128**, 043303 (2020).
[20] J. Hnilica, P. Klein, P. Vašina, R. Snyders, and N. Britun, J. Appl. Phys. **128**, 043304 (2020).
[21] A. D. Pajdarová, T. Kozák, J. Čapek, and T. Tölg, Plasma Sources Sci. Technol. **31**, 05LT04 (2022).
[22] D. Lundin, P. Larsson, E. Wallin, M. Lattemann, N. Brenning, and U. Helmersson, Plasma Sources Sci. Technol. **17**, 035021 (2008).

© Author(s) 2022

[23]A. Hecimovic and A. von Keudell, J. Phys. D: Appl. Phys. **51**, 453001 (2018).
[24]M. Rudolph, H. Hajihoseini, M. A. Raadu, J. T. Gudmundsson, N. Brenning, T. M. Minea, A. Anders, and D. Lundin, J. Appl. Phys. **129**, 033303 (2021).
[25]M. Rudolph, D. Kalanov, W. Diyatmika, and A. Anders, J. Appl. Phys. **130**, 243301 (2021).
[26]M. Panjan, R. Franz, and A. Anders, Plasma Sources Sci. Technol. **23**, 025007 (2014).
[27]D. J. Christie, J. Vac. Sci. Technol. A **23**, 330 (2005).
[28]A. Butler, N. Brenning, M. A. Raadu, J. T. Gudmundsson, T. Minea, and D. Lundin, Plasma Sources Sci. Technol. **27**, 105005 (2018).
[29]M. Rudolph, N. Brenning, M. A. Raadu, H. Hajihoseini, J. T. Gudmundsson, A. Anders, and D. Lundin, Plasma Sources Sci. Technol. **29**, 05LT01 (2020).
[30]H. Hajihoseini, M. Čada, Z. Hubička, S. Ünaldi, M. A. Raadu, N. Brenning, J. T. Gudmundsson, and D. Lundin, J. Vac. Sci. Technol. A **38**, 033009 (2020).
[31]J. Vlček and K. Burcalová, Plasma Sources Sci. Technol. **19**, 065010 (2010).
[32]M. Rudolph, N. Brenning, H. Hajihoseini, M. A. Raadu, J. Fischer, J. T. Gudmundsson, and D. Lundin, J. Vac. Sci. Technol. A **40**, 043005 (2022).
[33]S. P. Bugaev, N. N. Koval, N. S. Sochugov, and A. N. Zakharov, in *XVIIth International Symposium on Discharges and Electrical Insulation in Vacuum, July 21–26, 1996, Berkeley, California* (The Institute of Electrical and Electronics Engineers, Piscataway, NJ, 1996), pp. 1074–1076.
[34]A. Mishra, P. J. Kelly, and J. W. Bradley, Plasma Sources Sci. Technol. **19**, 045014 (2010).
[35]M. Rudolph, N. Brenning, H. Hajihoseini, M. A. Raadu, T. M. Minea, A. Anders, D. Lundin, and J. T. Gudmundsson, J. Phys. D: Appl. Phys. **55**, 015202 (2022).
[36]J. W. Bradley, A. Mishra, and P. J. Kelly, J. Phys. D: Appl. Phys. **48**, 215202 (2015).
[37]N. Brenning, A. Butler, H. Hajihoseini, M. Rudolph, M. A. Raadu, J. T. Gudmundsson, T. Minea, and D. Lundin, J. Vac. Sci. Technol. A **38**, 033008 (2020).
[38]N. Brenning, H. Hajihoseini, M. Rudolph, M. A. Raadu, J. T. Gudmundsson, T. M. Minea, and D. Lundin, Plasma Sources Sci. Technol. **30**, 015015 (2021).

© Author(s) 2022